Supplementary Notes

Supplementary Note 1. Wind exposure metrics

Sea-surface wind speed was obtained from the NOAA blended sea-surface wind product (Wallcraft et al. 2009), a global 0.25° latitude–longitude analysis that combines satellite scatterometer and radiometer retrievals, buoy observations and numerical weather-prediction output into monthly mean 10-m wind speed fields. For a bleaching observation at grid cell (i, j) recorded in month M of year Y, the k-month antecedent mean wind speed (k = 6, 12) was computed as the arithmetic mean of monthly wind speed over the k consecutive months ending in the survey month:

$$W_k(i,j) = (1/k)\,\Sigma_{n=0}^{k-1}\, W(Y-n,\, M-n,\, i,\, j).$$

The long-term background wind speed was computed as the mean of all N monthly fields available for the cell over the 1993–2020 reference period:

$$W\_LT(i,j) = (1/N)\,\Sigma_{y=1993}^{2020}\,\Sigma_{m=1}^{12}\, W(y,\, m,\, i,\, j).$$

Antecedent windows capture transient wind forcing in the months preceding a survey, whereas the long-term mean captures the persistent background regime that defines a site's chronic ventilation environment; the two are weakly correlated and were never entered in the same model. Wind metrics were joined to bleaching records by exact match on grid-cell coordinates and, for the antecedent windows, on survey month. The antecedent mean wind speed — the 6-month window in the global dataset and the 12-month window in the in-situ dataset, each selected by AIC (ΔAIC $\approx$ 20 favouring the 6-month window in the global dataset) — is the predictor entered in the models and referred to as sustained wind in the main text. The long-term 1993–2020 mean is retained only as a climatological reference; entered on its own it is not significantly associated with severity (odds ratio $\approx$ 1.08 per s.d., $P = 0.36$), whereas the 6-month antecedent mean is strongly protective (odds ratio $\approx$ 0.70, $P < 10^{-6}$), indicating that the association operates on a seasonal-to-annual rather than a decadal timescale.

Supplementary Note 2. Tropical-cyclone power: reconstruction and sensitivity

Tropical-cyclone tracks were taken from IBTrACS v4.01 (Knapp et al. 2010), which provides homogenized 6-hourly storm position, maximum sustained 10-m wind speed and central pressure for all basins. For each reef location we retained every 6-hourly track point within a radius of 400 km. At each retained point the local wind speed V(r) at radial distance r from the storm centre was reconstructed with a Holland-type parametric profile (Holland 1980):

$$V(r) = \sqrt{[\, B\,(\Delta P/\rho)\,(R_{max}/r)^{B}\, exp(-(R_{max}/r)^{B}) + (r\,f/2)^{2}\,]} - r\,f/2,$$

with central-pressure deficit $\Delta P = P_n - P\_c$ (ambient P_n = 1010 hPa), radius of maximum wind R_{max}, Holland shape parameter B = 1.5, air density ρ = 1.15 kg m^{-3} and Coriolis parameter $f = 2\Omega \sin\varphi$. When R_{max} or central pressure were missing from IBTrACS, R_{max} was set to 30 km and the radial field scaled to the reported maximum sustained wind with exponential decay beyond R_{max}. Tropical-cyclone power was accumulated as a power-dissipation–type quantity (Emanuel 2005), in which the cube of wind speed gives intense storms a dominant weight:

$$TCPower = \Sigma_i V_i^3 \Delta t_i , \quad \Delta t_i = 6\ h,$$

summed over all retained 6-hourly points within 400 km, over three windows: the 6 and 12 months preceding each observation, and cumulatively over 1993–2020 independent of survey date. Sensitivity tests varied the influence radius (200, 300, 400 km), the shape parameter B (1.3–1.8) and the default R_{max} (20–40 km). Smaller radii and larger B reduced absolute TCPower but left the rank ordering of reef sites and the sign and significance of the TCPower–severity relationship unchanged; cumulative TCPower at reef sites therefore reflects storm frequency and intensity rather than the parametric assumptions of the reconstruction.

Supplementary Note 3. Box Upwelling–Diffusion (BUD) model

The wind–Ω relationship was interpreted with a steady-state Box Upwelling–Diffusion (BUD) model in the tradition of box-diffusion ocean–carbon models (Hoffert et al. 1981). A single well-mixed surface box — the mixed ocean layer (MOL) of thickness h = 40 m — exchanges dissolved inorganic carbon (DIC), total alkalinity (TA) and calcium with a fixed deep reservoir through wind-driven upwelling (velocity W) and vertical turbulent diffusion (eddy diffusivity A_z acting over thickness h), while exchanging CO_2 with the atmosphere (flux Fa) and removing carbon by biological export (B), partitioned between organic matter and $CaCO_3$. The carbonate system, including aragonite saturation state Ωarag, was evaluated from box TA and DIC with the seacarb package (Lavigne & Gattuso 2012) using the CO_2 solubility of Weiss (1974). Parameter values follow the reference implementation used to generate the results (Supplementary Code) and are listed in Supplementary Table 1.

Wind scaling.

Upwelling, diffusivity and biological export were each scaled to wind speed U relative to a reference trade-wind speed U* = 6 m s^{-1} through independent power-law exponents m, q and n:

$$W(U) = W_0 (U/U^*)^m , \quad A_z(U) = A_{z0} (U/U^*)^q , \quad B(U) = B_0 (U/U^*)^n ,$$

with the combined vertical exchange rate M = W + A_z/h. The air–sea CO_2 flux used a quadratic gas-transfer velocity k = αU^2 (Wanninkhof 2014; Schmidt number 660), Fa = ρ k K_0 (Pa − Pw), where Pa is atmospheric and Pw the box CO_2 partial pressure. Biological export was split as F_org = −(1−r_$CaCO_3$)B and F_$CaCO_3$ = −r_$CaCO_3$ B (negative denoting removal from the MOL).

Steady-state balances.

Setting the surface-box tendencies to zero gives the MOL concentrations as deviations from the deep reservoir:

$$DIC\_MOL = DIC\_deep + (F\_org + F\_CaCO_3 + Fa)/(\rho M),$$
$$TA\_MOL = TA\_deep + (2 F\_CaCO_3 + r\_N F\_org^{prod})/(\rho M), \quad Ca\_MOL = Ca\_deep + F\_CaCO_3/(\rho M),$$

where r_N = 16/106 is the nitrate-to-carbon alkalinity contribution of organic production. Because Fa itself depends on Pw, the box pCO_2 was solved self-consistently for each U (root-finding on the residual between the carbonate-system pCO_2 and the assumed Pw), after which

Ωarag was returned by seacarb. Carbon-budget closure (Fa + Fup + Fd − B ≈ 0) was confirmed at every solution.

Parameter grid and the three reported cases.

The model was run for U = 1–10 m s^{-1} over the full grid m, n, q ∈ {0, 1, 2} (27 combinations). For the main-text figure we report three cases that bracket the plausible coupling of the surface carbon budget to wind while holding diffusivity wind-independent (q = 0), the latter justified by the limited variability of turbulent diffusion across the Pacific pycnocline (Itoh et al. 2021): (i) m = n = q = 0, in which neither upwelling nor productivity responds to wind; (ii) m = n = 1, q = 0; and (iii) m = n = 2, q = 0, the last corresponding to an Ekman-type response in which wind-driven transport scales with wind stress (U^2). We set n = m because, in the open ocean, biological export is supplied largely by upwelled nutrients, so productivity and upwelling are expected to co-vary; the cases n = m = 0 and n = m = 2 then bracket the realistic intermediate behaviour, and q = 0 isolates the role of advective/productive coupling from diffusive change.

Result and comparison with observations.

Across these cases the modelled steady-state dependence of surface Ωarag on wind speed rises from essentially flat (slightly negative, −0.001 per m s^{-1}) at m = n = 0 to weakly positive at m = n = 1 (+0.028 per m s^{-1}) and m = n = 2 (+0.036 per m s^{-1}). In no case does the model produce the strong negative Ω–wind relationship that would be expected if wind simply upwelled carbon-rich, low-Ω water; instead, the wind-driven increase in both CO_2 outgassing capacity and biological drawdown offsets the upwelling supply of DIC, leaving a weak positive net dependence. This reproduces the sign and approximate magnitude of the observed relationship. In the reef observations the Ω–wind slope is +0.019 per m s^{-1} at the surface (0 m; Pearson r = +0.15) and +0.099 per m s^{-1} at 50 m (r = +0.38). The modelled slope (+0.03 to +0.04) lies between these and is closer to the subsurface value, as expected because the BUD box represents an integrated mixed ocean layer rather than the skin surface; tropical mixed-layer depth is typically ~30–50 m (de Boyer Montégut et al. 2004), so the 50-m observations are the more appropriate comparison and there the positive relationship is clearest. We emphasize that the aragonite-saturation fields are gridded at ~1° (~100 km), coarser than the 0.25° wind product, so the wind–Ω relationship is treated as a long-term climatological association rather than an event-scale one; this resolution mismatch, together with the use of fixed deep-reservoir end-members, is the main source of quantitative uncertainty in the comparison. Finer-scale carbonate-chemistry products, as they become available, could test this wind–Ω association at reef-relevant scales.

Supplementary Table 1. BUD model constants (reference implementation).

Symbol	Value	Meaning
ρ	1025 kg m^{-3}	seawater density
h	40 m	mixed ocean layer (MOL) thickness
S, T	35, 25 °C	salinity, temperature
TA_deep	2350 µmol kg^{-1}	deep total alkalinity
DIC_deep	2100 µmol kg^{-1}	deep dissolved inorganic carbon
Ca_deep	10.3 mmol kg^{-1}	deep calcium

U*	6 m s^{-1}	reference (trade-wind) speed
W_0	4.7×10^{-7} m s^{-1}	upwelling velocity at U*
A_{z0}	1×10^{-5} m^2 s^{-1}	vertical eddy diffusivity at U*
B_0	32.4×10^{-9} mol C m^{-2} s^{-1}	biological export at U*
r_$CaCO_3$	0.07	$CaCO_3$ fraction of export
r_N	16/106	nitrate alkalinity per organic C
α	6.97×10^{-7} m s^{-1} per U^2	gas-transfer coefficient (Wanninkhof 2014)
Pa	430 µatm	atmospheric pCO_2
K_0	2.85×10^{-2} mol kg^{-1} atm^{-1}	CO_2 solubility (Weiss 1974)

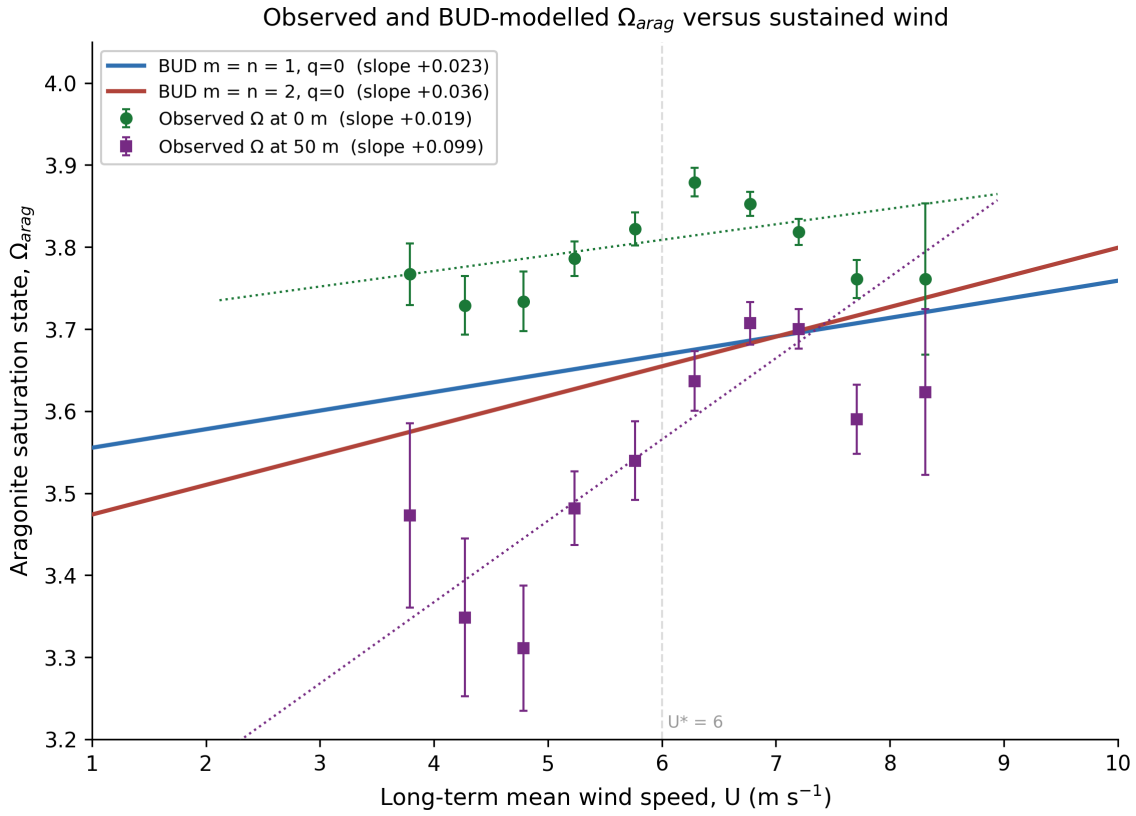

Supplementary Figure 1. Observed and BUD-modelled aragonite saturation state (Ωarag) versus sustained background wind. Observed Ωarag at 0 m (green circles) and 50 m (purple squares), from an observation-based gridded product, binned by long-term mean wind speed (0.5 m s^{-1} bins, 2–9 m s^{-1}; mean ± 95% confidence interval) with least-squares fits (dotted). Both depths show a weak positive Ω–wind relationship, stronger at 50 m (slope +0.099 per m s^{-1}) than at the surface (+0.019 per m s^{-1}). Solid lines are linear fits to the steady-state Box Upwelling–Diffusion (BUD) model (Supplementary Note 3) for the two physically plausible wind-coupling cases: upwelling and productivity scaling linearly (m = n = 1; blue) and quadratically (m = n = 2; red) with wind, vertical diffusivity held wind-independent (q = 0; Itoh et al. 2021). The model reproduces the weak positive sensitivity of Ω to wind and excludes the strong negative relationship expected if wind-driven upwelling of carbon-rich, low-Ω water dominated; the m = n = 2 slope (+0.036 per m s^{-1}) best matches the data. Because the BUD box represents an integrated mixed ocean

layer (~30–50 m; de Boyer Montégut et al. 2004), the modelled curves fall between the 0 m and 50 m observations.

Supplementary Note 4. Shapley decomposition of explained variation

To attribute McFadden's pseudo-R^2 among predictor groups while respecting within-group collinearity, we used a Shapley decomposition (Shapley 1953; Grömping 2007) at the level of predictor groups rather than individual coefficients. McFadden's pseudo-R^2 (McFadden 1974) for a fitted ordinal model is $R^2 = 1 - \ell(\text{model})/\ell(\text{null})$, with ℓ the maximized log-likelihood and the null model containing only the cumulative-logit thresholds. For G mutually exclusive groups, the Shapley value of group g is its average marginal contribution to R^2 over all orderings of the groups:

$$\varphi_g = \Sigma_{S \subseteq G \setminus \{g\}} [\, |S|!(|G|-|S|-1)! / |G|! \,] [\, R^2(S \cup \{g\}) - R^2(S) \,].$$

With at most four groups the 2^G subset models were enumerated and fitted exactly, so no Monte-Carlo sampling was required; the resulting Shapley values are additive and sum to the full-model R^2, and the decomposition is order-independent. Groups were: for the global dataset, Thermal (degree-heating weeks and the three SST principal components), Wind (6-month antecedent mean wind), Cyclone (cumulative tropical-cyclone power) and Other site descriptors (distance to shore, turbidity and exposure); for the in-situ dataset, Thermal (degree-heating weeks, diurnal temperature range, rate of temperature change, acute stress and thermal trajectory), Depth and Wind. Uncertainty in each group's share was obtained by bootstrap resampling of grid cells for the global dataset. For the within-region variant, marine-realm indicators (Spalding et al. 2007) were included in the null model and in every subset model, so that the decomposition partitions only the deviance explained beyond region; this confirmed that the wind share is not inflated by between-region structure. The within-region estimators themselves (realm fixed effects and the Mundlak within–between decomposition; Mundlak 1978; Bell & Jones 2015) are described in the main-text Methods.

Supplementary Note 5. Boundary-layer scaling of ROS clearance

This note supports the mechanistic interpretation presented in the Discussion and Fig. 5. It is intended as a scaling argument rather than a fitted component of the statistical analysis and should therefore be viewed as a leading hypothesis consistent with the data and with controlled flow experiments, rather than as a mechanism demonstrated directly by the present study. Direct field evidence linking sustained background wind, as distinct from local waves and currents, to diffusive-boundary-layer thickness and reactive-oxygen-species (ROS) efflux at bleaching-relevant scales remains limited.

Export of reactive oxygen species (for example, H_2O_2) from coral tissue to the overlying water is constrained by molecular diffusion across the diffusive boundary layer (DBL). The diffusive flux is

$$J = k\,(C_t - C_\infty), \quad k = D/\delta,$$

where C_t and C_∞ are tissue-surface and free-stream concentrations, k is the mass-transfer coefficient, D the molecular diffusivity and δ the DBL thickness. Mass transfer over the colony is

described by the Sherwood number Sh = kL/D, related to flow through Sh = a·Re^m·Sc^n, with Reynolds number Re = U_flow L/ν, Schmidt number Sc = ν/D, characteristic colony length L and kinematic viscosity ν. Hence k ∝ U_flow^m, and because near-tissue flow scales with surface wind as U_flow ∝ U^p, the clearance rate scales as

$$k \propto U^{(m \cdot p)}.$$

The exponent m encodes the hydrodynamic regime and surface character (m ≈ 0.5 for smooth surfaces in laminar–transitional flow; m ≈ 0.8–1.0 for rough, branching morphologies in turbulent flow), while p ranges from ≈ 0.5–1 where near-surface flow is wave-dominated and only weakly wind-coupled, to ≈ 2 where direct wind stress (τ ∝ U^2) drives the near-tissue flow. The composite exponent m·p therefore spans roughly 0.5 to 2. We adopt this range rather than a single value because the morphological coefficient a and the regime exponents vary among coral taxa and habitats, with branching and tabular corals expected to clear reactive oxygen species more efficiently per unit wind than massive or encrusting forms (Nakamura 2010).

Supplementary Note 6. Projected change in mean wind speed over coral reefs (CMIP6)

Trade winds are broadly expected to weaken under warming, but how that change is expressed at reef locations is not established. Rather than assume a uniform decline, we characterise the full distribution of projected wind change over reef area and ask two questions: whether mean winds decline or intensify over coral reefs and what the net change is (Q1), and how large the change is, how it is distributed and what it implies for severe-bleaching odds (Q2).

Data and ensemble construction.

We use monthly mean near-surface wind speed (`sfcWind`, table `Amon`) from the full available CMIP6 ensemble (Eyring et al. 2016), read directly from the Pangeo Google-Cloud Zarr archive. For each model we compute the change in the climatological mean between 2080–2099 and 1995–2014, ΔU, on the model's native grid, under SSP2-4.5 and SSP5-8.5 (O'Neill et al. 2016). One realisation is retained per model (preferring `r1i1p1f1`, otherwise the lowest forcing variant; native grid `gn` preferred, with fallback to `gr`/`gr1`), yielding 43 models for SSP5-8.5 and 41 for SSP2-4.5. Relaxing the earlier `r1i1p1f1`-only selection recovers the f2/f3-forcing models (UKESM1-0-LL, HadGEM3-GC31, the CNRM family, MIROC-ES2L) and the regridded-only models (EC-Earth3, GFDL, IPSL, INM, KIOST). The realisation and grid label retained for every model are listed in Supplementary Table 2.

Reef sampling.

ΔU is sampled by nearest grid cell at all 63,496 equal-area 5×5 km reef polygons. Because the cells are equal-area, a plain mean or histogram over them is the reef-area-weighted quantity, so no de-clustering correction is needed. One ΔU column per model is written beside the coordinates, with ensemble summaries, in the accompanying data table (Supplementary Code).

Model independence.

The 43 models derive from 26 institutions (Supplementary Table 2) and fewer independent atmospheric formulations: the CAM/CESM lineage supplies nine models and the

UK Met Office UM/HadGEM lineage six, so roughly a third of the ensemble reflects two atmospheric models (Knutti et al. 2013). We therefore report the reef-area-mean both one-model-one-vote and one-centre-one-vote (averaged within institution, then across institutions). The two weightings agree in sign and magnitude (SSP5-8.5: −0.016 versus −0.008 m s^{-1}; SSP2-4.5: +0.007 versus +0.013 m s^{-1}), indicating the central estimate is robust to model genealogy.

Results: distribution and robustness.

Under SSP5-8.5, mean winds weaken over 58.8% of reef area, but the net change is small (area-mean ΔU −0.016 m s^{-1}; area-weighted median −0.020; 5th–95th percentile −0.225 to +0.191 m s^{-1}) and of limited robustness: at least 66% of models agree on a decline over only 26.4% of reef area, and at least 80% agree on the sign over only 19.4%. A two-thirds threshold (66%) is commonly used as an indicator of moderate model agreement in CMIP ensemble analyses. Under SSP2-4.5 the net change is indistinguishable from zero (area-weighted median −0.002 m s^{-1}; 51.1% of area declining). The small area-mean reflects cancellation of sizeable regional declines and increases rather than a consensus of no change, so the decisive diagnostic is the sign-agreement fraction, not the mean. The higher-emissions scenario shows slightly more reef-wind weakening than the moderate one, consistent with a stronger forced slackening of the trade winds. We note that CMIP6 models share known biases in the simulation of tropical circulation, including the projected weakening of the Pacific Walker cell, so these wind projections carry structural as well as scenario uncertainty; this reinforces our treatment of the net change as a low-confidence, spatially variable tendency rather than a robust trend.

Translation to severe-bleaching odds.

Per-reef ΔU is converted to a change in severe-bleaching odds using the GLO within-region 6-month wind coefficient (odds ratio ≈ 0.70 per s.d.; s.d. ≈ 1.2 m s^{-1}; van Woesik & Kratochwill 2022), the conceptual match to a sustained multidecadal change in climatological mean wind. Because the fitted sensitivity derives from the 6-month antecedent wind whereas the projected change is in the multidecadal climatological mean, this translation applies the antecedent coefficient as a conceptual proxy rather than a like-for-like predictor; given that the long-term mean wind is itself only weakly related to severity in our data, the projected odds changes should be read as indicative of direction and relative magnitude rather than as calibrated forecasts. At the area-mean the implied change is +0.6% (SSP5-8.5) and −0.2% (SSP2-4.5); at the most strongly wind-declining reefs it reaches +19% (SSP5-8.5; ΔU ≈ −0.58 m s^{-1}) and +8.5% (SSP2-4.5). The steeper SAF 12-month coefficient (odds ratio ≈ 0.45 per s.d.; Safaie et al. 2018) gives roughly 2–2.5× these values — up to ≈ +47% (SSP5-8.5) and +20% (SSP2-4.5) at the extreme — and is reported as a sensitivity bracket rather than a co-equal map, because its event-window provenance (n = 81) makes a multidecadal climatological projection an over-extension if presented as an independent estimate. The change in severe-bleaching odds is mapped in main-text Fig. 6 (GLO model); Supplementary Figure 2 shows both scenarios and the ΔU distribution. For each reef the odds multiplier is the per-standard-deviation odds ratio raised to the standardized wind change, (OR)^(ΔU/σ), with σ the across-reef standard deviation of background wind; for completeness, the SAF area-mean change is ≈ +1.5% (SSP5-8.5), with a per-reef 5th–95th-percentile range of roughly −12% to +16%.

a GLO odds change, SSP5-8.5

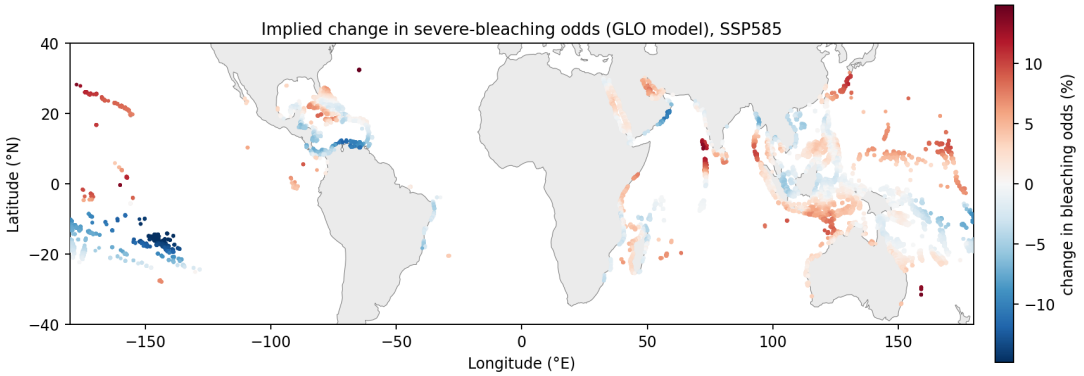

b GLO odds change, SSP2-4.5

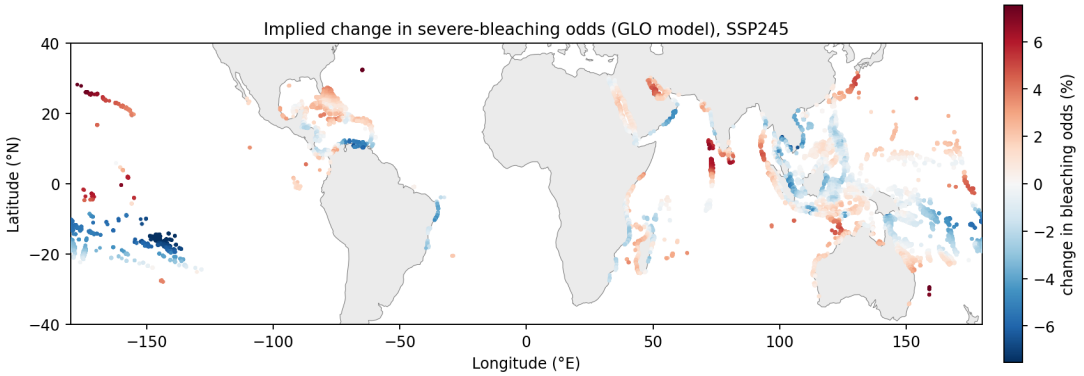

c Distribution of per-reef ΔU, SSP5-8.5

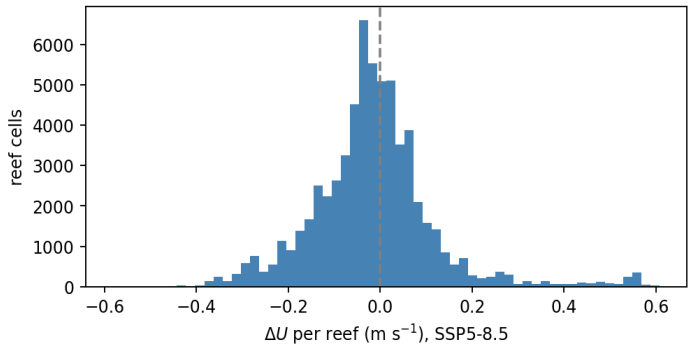

Supplementary Figure 2*. Implied change in severe-bleaching odds and the ΔU distribution.* (a,b) Per-reef change in severe-bleaching odds from projected ΔU using the GLO 6-month wind coefficient, for SSP5-8.5 and SSP2-4.5; red, higher odds (weakening winds); blue, lower odds (strengthening winds); continental outlines from Natural Earth. (c) Distribution of ensemble-mean ΔU across all 63,496 reef cells under SSP5-8.5, with the mode just below zero and a heavier negative tail. The SAF coefficient gives roughly 2–2.5× the odds amplitude of GLO and is reported as a sensitivity bracket above.

Supplementary Table 2*. CMIP6 models, realisations and grids used in the wind-projection analysis (SSP5-8.5).*

source_id	institution_id	member_id	grid

ACCESS-CM2	CSIRO-ARCCSS	r1i1p1f1	gn
ACCESS-ESM1-5	CSIRO	r1i1p1f1	gn
AWI-CM-1-1-MR	AWI	r1i1p1f1	gn
BCC-CSM2-MR	BCC	r1i1p1f1	gn
CAMS-CSM1-0	CAMS	r1i1p1f1	gn
CAS-ESM2-0	CAS	r1i1p1f1	gn
CESM2	NCAR	r4i1p1f1	gn
CESM2-WACCM	NCAR	r1i1p1f1	gn
CMCC-CM2-SR5	CMCC	r1i1p1f1	gn
CMCC-ESM2	CMCC	r1i1p1f1	gn
CNRM-CM6-1	CNRM-CERFACS	r1i1p1f2	gr
CNRM-CM6-1-HR	CNRM-CERFACS	r1i1p1f2	gr
CNRM-ESM2-1	CNRM-CERFACS	r1i1p1f2	gr
CanESM5	CCCma	r1i1p1f1	gn
CanESM5-CanOE	CCCma	r1i1p2f1	gn
E3SM-1-1	E3SM-Project	r1i1p1f1	gr
EC-Earth3	EC-Earth-Consortium	r1i1p1f1	gr
EC-Earth3-CC	EC-Earth-Consortium	r1i1p1f1	gr
EC-Earth3-Veg	EC-Earth-Consortium	r1i1p1f1	gr
EC-Earth3-Veg-LR	EC-Earth-Consortium	r1i1p1f1	gr
FGOALS-f3-L	CAS	r1i1p1f1	gr
FGOALS-g3	CAS	r1i1p1f1	gn
FIO-ESM-2-0	FIO-QLNM	r1i1p1f1	gn
GFDL-CM4	NOAA-GFDL	r1i1p1f1	gr1

GFDL-ESM4	NOAA-GFDL	r1i1p1f1	gr1
GISS-E2-1-G	NASA-GISS	r1i1p3f1	gn
HadGEM3-GC31-LL	MOHC	r1i1p1f3	gn
HadGEM3-GC31-MM	MOHC	r1i1p1f3	gn
IITM-ESM	CCCR-IITM	r1i1p1f1	gn
INM-CM4-8	INM	r1i1p1f1	gr1
INM-CM5-0	INM	r1i1p1f1	gr1
IPSL-CM6A-LR	IPSL	r1i1p1f1	gr
KACE-1-0-G	NIMS-KMA	r1i1p1f1	gr
KIOST-ESM	KIOST	r1i1p1f1	gr1
MIROC-ES2L	MIROC	r1i1p1f2	gn
MIROC6	MIROC	r1i1p1f1	gn
MPI-ESM1-2-HR	MPI-M	r1i1p1f1	gn
MPI-ESM1-2-LR	MPI-M	r1i1p1f1	gn
MRI-ESM2-0	MRI	r1i1p1f1	gn
NorESM2-LM	NCC	r1i1p1f1	gn
NorESM2-MM	NCC	r1i1p1f1	gn
TaiESM1	AS-RCEC	r1i1p1f1	gn
UKESM1-0-LL	MOHC	r1i1p1f2	gn

Total: 43 models from 26 institutions. SSP2-4.5 uses the same set minus ACCESS-ESM1-5 and HadGEM3-GC31-MM (41 models). Datasets were read from the Pangeo CMIP6 Zarr archive (`gs://cmip6/CMIP6/…`).

Supplementary Note 7. Robustness of the wind association.

The global analysis retains one bleaching record per 5 × 5 km reef site (sites ≥ 5 km apart); the 0.25° grid is used only to attach the gridded SST and wind fields, so several sites can fall within one 0.25° wind/SST cell (275 of 835 occupied cells contain ≥ 2 sites, which therefore

share identical gridded predictors). To confirm that the wind association is not an artefact of this shared structure, we refitted the ordinal model (i) with a cluster bootstrap that resamples whole 0.25° cells and (ii) after collapsing to a single (earliest) record per 0.25° cell. The 6-month antecedent-wind odds ratio is essentially unchanged under both (Supplementary Table 3). We additionally compared antecedent windows: the protective association is strongest for the 6-month mean, weaker for the 12-month mean, and absent for the long-term 1993–2020 mean, consistent with a seasonal-to-annual rather than decadal mechanism.

Supplementary Table 3. Robustness of the GLO 6-month-wind odds ratio.

Model variant	*n*	Wind OR (per s.d.)	95% CI
Pooled OLR, all sites (reported)	1,195	0.70	0.61–0.80
Cluster bootstrap by 0.25° cell	1,195	0.70	0.58–0.80
One record per 0.25° cell (earliest)	833	0.67	0.57–0.79

Wind-window comparison (same controls; all odds ratios per s.d.): 6-month OR = 0.70 ($P < 10^{-6}$); 12-month OR = 0.85 ($P = 0.02$); long-term (1993–2020) OR = 1.08 ($P = 0.36$).

Supplementary References

Cited across Supplementary Notes 1–7, in author–year style consistent with the notes. Individual CMIP6 dataset DOIs can be exported from the WCRP CMIP6 citation service.

Bell, A. & Jones, K. Explaining fixed effects: random effects modeling of time-series cross-sectional and panel data. *Polit. Sci. Res. Methods* 3, 133–153 (2015).

de Boyer Montégut, C., Madec, G., Fischer, A. S., Lazar, A. & Iudicone, D. Mixed layer depth over the global ocean: an examination of profile data and a profile-based climatology. *J. Geophys. Res.* 109, C12003 (2004).

Emanuel, K. Increasing destructiveness of tropical cyclones over the past 30 years. *Nature* 436, 686–688 (2005).

Eyring, V. *et al.* Overview of the Coupled Model Intercomparison Project Phase 6 (CMIP6) experimental design and organization. *Geosci. Model Dev.* 9, 1937–1958 (2016).

Grömping, U. Estimators of relative importance in linear regression based on variance decomposition. *Am. Stat.* 61, 139–147 (2007).

Hoffert, M. I., Callegari, A. J. & Hsieh, C.-T. A box-diffusion carbon-cycle model with upwelling, polar bottom-water formation and a marine biosphere. In *Carbon Cycle Modelling (SCOPE 16)* (ed. Bolin, B.) 287–305 (Wiley, 1981).

Holland, G. J. An analytic model of the wind and pressure profiles in hurricanes. *Mon. Weather Rev.* 108, 1212–1218 (1980).

Itoh, S. *et al.* Vertical turbulent diffusivity across the Pacific pycnocline. (2021).

Knapp, K. R., Kruk, M. C., Levinson, D. H., Diamond, H. J. & Neumann, C. J. The International Best Track Archive for Climate Stewardship (IBTrACS). *Bull. Am. Meteorol. Soc.* 91, 363–376 (2010).

Knutti, R., Masson, D. & Gettelman, A. Climate model genealogy: generation CMIP5 and how we got there. *Geophys. Res. Lett.* 40, 1194–1199 (2013).

Lavigne, H. & Gattuso, J.-P. seacarb: seawater carbonate chemistry with R. R package (2012).

McFadden, D. Conditional logit analysis of qualitative choice behavior. In *Frontiers in Econometrics* (ed. Zarembka, P.) 105–142 (Academic Press, 1974).

Mundlak, Y. On the pooling of time series and cross section data. *Econometrica* 46, 69–85 (1978).

Nakamura, T. Importance of water flow on the physiological responses of reef-building corals. *Galaxea* 12, 1–14 (2010).

O'Neill, B. C. *et al.* The Scenario Model Intercomparison Project (ScenarioMIP) for CMIP6. *Geosci. Model Dev.* 9, 3461–3482 (2016).

Safaie, A. *et al.* High frequency temperature variability reduces the risk of coral bleaching. *Nat. Commun.* 9, 1671 (2018).

Shapley, L. S. A value for n-person games. In *Contributions to the Theory of Games II* (eds Kuhn, H. W. & Tucker, A. W.) 307–317 (Princeton Univ. Press, 1953).

Spalding, M. D. *et al.* Marine ecoregions of the world: a bioregionalization of coastal and shelf areas. *BioScience* 57, 573–583 (2007).

van Woesik, R. & Kratochwill, C. A global coral-bleaching database, 1980–2020. *Sci. Data* 9, 20 (2022).

Wallcraft, A. J. *et al.* Comparisons of monthly mean 10-m wind speed from satellite and NWP products over the global ocean. *J. Geophys. Res.* 114, D16109 (2009).

Wanninkhof, R. Relationship between wind speed and gas exchange over the ocean revisited. *Limnol. Oceanogr. Methods* 12, 351–362 (2014).

Weiss, R. F. Carbon dioxide in water and seawater: the solubility of a non-ideal gas. *Mar. Chem.* 2, 203–215 (1974).

Natural Earth. Free vector and raster map data, naturalearthdata.com (110 m land/coastline).